

TDOA Prior Based Contrast Source Inversion for Microwave Ablation Zone Quantitative Imaging

Hideaki Muramatsu, *Student member, IEEE*, and Shouhei Kidera, *Senior Member, IEEE*

Abstract—This study presents an efficient quantitative microwave imaging method for ablation zones in microwave breast cancer treatment. To maintain an accurate estimate of complex permittivity changes during the ablation process, we integrate the time of difference of arrival (TDOA) based ablation boundary prior into the contrast source inversion (CSI) based nonlinear inverse scattering framework. This incorporation mitigates the ill-posed problem of the original CSI scheme by restricting the region of interest (ROI) using the TDOA prior. Specifically, by focusing on the characteristics of the CSI cost function, our approach simultaneously determines an appropriate ablation boundary and the temporal decrease of complex permittivity, which is closely correlated with the temperature change of the ablated tissue. The effectiveness of our proposed scheme is validated using the two-dimensional finite difference time domain method with realistic breast phantoms, demonstrating accurate dielectric profile reconstruction.

Index Terms—Microwave ablation (MWA), Breast cancer treatment, Complex permittivity imaging, Non-linear inverse scattering, time difference of arrival (TDOA), contrast source inversion (CSI).

I. INTRODUCTION

Microwave ablation (MWA) is a highly promising tool achieving minimally invasive cancer treatments. Microwave-frequency radiation exhibits a capacity to heat cells more rapidly than lower radio-frequency radiation [1]. Numerous studies highlight the efficacy of MWA as a safe and reliable treatment, particularly for liver tumors [2], as well as for other types of cancer, such as kidney and breast tumors. Specifically for breast cancer ablation, MWA considerably reduces the physical and mental burdens on patients by eliminating the need for large-scale removal of breast tissue. However, to ensure the safe and effective ablation of malignant tumors without harming healthy tissues, integrating MWA with an appropriate imaging scheme is imperative. Magnetic resonance imaging (MRI) [3], [4] and ultrasound-based imaging have been developed and demonstrated as suitable modalities [5]–[8]. While MRI offers high spatial resolution, it typically struggles to maintain sufficient temporal resolution and involves the use of large-scale and expensive equipment. Ultrasound imaging equipment is less expensive and more compact than MRI equipment; however, the microbubbles caused by tissue hydration can contaminate the contrast image [9].

This work was supported by JSPS KAKENHI Grant Number JP23K26113 and the Asahi Glass Foundation, Continuation Grants for Young Researchers.

The authors are with the Graduate School of Informatics and Engineering, University of Electro-Communications, Tokyo, 1828585, Japan (kidera@uec.ac.jp).

As a promising alternative, microwave-based ablation monitoring offers numerous advantages, such as safety, rapid measurement, and compatibility with MWA equipment. Notably, the dielectric properties of tissues at microwave frequencies are highly sensitive to temperature and physiological state [10]. This means that ablated tissues, which become hydrated, exhibit a considerable decrease in complex permittivity when exposed to microwave radiation [11], [12]. Leveraging these characteristics, the evolution of ablated tissue can be quickly monitored by measuring the forward-scattered components received by an external antenna from an interstitial MWA source, with the temporal differences in signals being appropriately processed. Several studies have focused on reconstructing the dielectric profile of the ablation zone using inverse scattering (*i.e.*, tomography) approaches, most of which assume relatively homogeneous media, such as in liver cancer treatment [13]–[15]. However, these approaches are not suitable for heterogeneous media, such as the breast, and involve high computational costs. To address these challenges, researchers [16]–[18] have proposed a full-wave inversion scheme based on the Born iterative approach, which focuses on the temporal difference in scattering signals between pre-ablation and during ablation. However, this method requires multiple transmitters and receivers in the surrounding area, resulting in a complex and expensive measurement configuration.

In contrast, previous studies [19], [21] have focused on a more simplified configuration where an interstitial MWA source acts as the transmitter, and multiple receivers are located externally around the breast, requiring only passive sensors to monitor the ablation zone. These approaches evaluate the time-difference-of-arrival (TDOA) of the forward-scattering signal from the internal MWA probe during pre-ablation and ablation states. This scheme is promising because it requires minimal prior knowledge, *i.e.*, only an estimate of the tissue's relative permittivity in the local treatment zone and its variation during ablation. Furthermore, it relies on a much simpler signal processing scheme. Previous studies [19] have demonstrated that this approach achieves real-time 3-D imaging of the ablation zone with acceptable reconstruction accuracy. However, accurate prior knowledge of the temporal changes in the dielectric constant in the ablation zone is required in this scheme, which is challenging to maintain even with a temperature monitoring tool along the MWA probe.

To address this issue, this paper introduces a TDOA prior-based inverse scattering approach using contrast source inver-

sion (CSI) [20] to maintain a heterogeneous dielectric profile of the ablation zone with less complexity, assuming a single internal source model. Notably, when assuming the single-source model, inverse scattering approaches are predicted to suffer from inaccuracies owing to severe ill-posed conditions compared to the multiple-source model described in a previous study [16]. To alleviate this issue, the TDOA-based ablation zone estimate is used to limit the region of interest (ROI), which helps reduce the number of unknowns, thereby easing the ill-posed condition. In the proposed scheme, the rate of decrease of the complex permittivity in the ablation zone is optimized by minimizing the cost function of the CSI, where only the total fields are updated to reduce the number of unknowns. Because the TDOA-based boundary estimation includes some errors, even with an accurate drop rate or average velocity, we independently optimize the drop rates for the TDOA boundary estimation and the CSI-based complex permittivity estimation.

The main contributions of this paper are summarized as follows.

- 1) In the proposed method, we employ the dual-variable optimization approach to provide the temporal variation of the complex permittivity during the ablation by integrating the TDOA-based ROI and CSI schemes. We use one variable to estimate the complex permittivity drop rate, and another one to determine the ablation zone using the TDOA method; these two variables are independently optimized to minimize the CSI cost function.
- 2) This scheme is applicable to a passive observation model, where an internal MWA probe is treated as a single transmitter.
- 3) The ill-posed condition is alleviated by introducing an ROI limitation into the CSI scheme, where only the total fields are updated with a fixed contrast function to prevent an local optimal solution. Additionally, the optimal ROI is determined by minimizing the cost function of CSI across multiple candidates using TDOA boundary outputs.
- 4) The CSI based total field optimization in the proposed scheme has the advantage over the FDTD based approach, in terms of computational complexity. where the optimal ROI is also determined by minimizing the cost function of CSI across multiple candidates using TDOA boundary outputs.

Notably, the first of the above contributions is the main difference from our previously published work [22], which employed a single-valuable optimization and could not simultaneously provide an accurate estimate for both the complex permittivity drop rate and the ablation boundary. Numerical validation using the two-dimensional (2-D) FDTD method with an MRI-derived realistic breast phantom demonstrates that our proposed scheme successfully reconstructs complex permittivity changes from the pre-ablation state with considerably higher accuracy compared to the original CSI scheme.

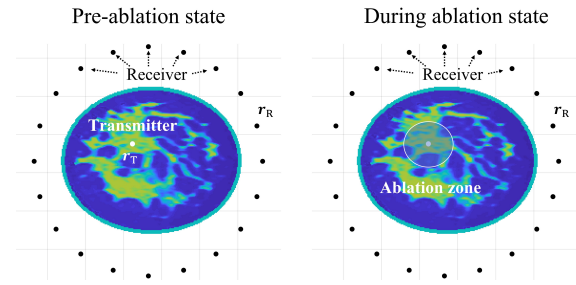


Fig. 1: Observation model and data acquisition configuration. Pre-ablation and during ablation states.

II. METHOD

A. Observation Model

Figure 1 illustrates the observation strategy for MWA monitoring. Multiple receivers positioned around the external area of the breast record the electric field from an interstitial source while the MWA probe is inserted into the cancer tissue. The total electric fields before and during the ablation are denoted as $e_{\text{pre}}^T(t; \mathbf{r}_T, \mathbf{r}_R)$ and $e_{\text{dur}}^T(t; \mathbf{r}_T, \mathbf{r}_R)$ with time t , respectively, where \mathbf{r}_T and \mathbf{r}_R are the locations of the transmitter and receiver, respectively. Ω_S denotes the observation area, including the receiver positions (\mathbf{r}_R). Ω_D denotes the area including a whole of breast media.

B. TDOA-based Boundary Estimation

Previous study [19] have proposed a low-complexity boundary estimation method for the evolving ablation zone using the TDOA values between pre-ablation and during-ablation states. This method relies on the propagation time from the internal transmitter to multiple receivers. It is based on the previous investigations that the relative permittivity of the ablation area considerably decreases owing to tissue dehydration, resulting in an earlier time-of-arrival (TOA) during ablation compared to pre-ablation. This occurs because lower permittivity increases the propagation speed of electromagnetic waves. The difference in TOA, denoted as $\Delta\tau$ is formulated as follows:

$$\begin{aligned} \Delta\tau(\mathbf{r}_R) &\equiv \tau_{\text{pre}}(\mathbf{r}_R) - \tau_{\text{dur}}(\mathbf{r}_R) \\ &\simeq (1 - \sqrt{\xi})\tau(\mathbf{r}_R; \mathbf{r}_A), \end{aligned} \quad (1)$$

Here $\tau(\mathbf{r}_R; \mathbf{r}_A)$ is the propagation time from \mathbf{r}_T (source location) to the receiver point \mathbf{r}_R via the ablation boundary point \mathbf{r}_A . We assume that the locations of \mathbf{r}_T , \mathbf{r}_A , and \mathbf{r}_R are on the same straight line. Figure 2 provides a conceptual illustration of the TDOA-based boundary estimation. The drop rate of relative permittivity is introduced as $\xi \equiv \bar{\epsilon}_{\text{dur}}/\bar{\epsilon}_{\text{pre}}$, where $\bar{\epsilon}_{\text{pre}}$ and $\bar{\epsilon}_{\text{dur}}$ are the averaged relative permittivities in the assumed ablation zone. By obtaining $\Delta\tau(\mathbf{r}_R)$, the ablation boundary point corresponding to the receiver location \mathbf{r}_R , denoted as $\mathbf{r}_A(\mathbf{r}_R)$, is determined as follows:

$$\mathbf{r}_A(\mathbf{r}_R) = \mathbf{r}_T + \frac{\bar{v}_{\text{pre}}\Delta\tau(\mathbf{r}_R)}{1 - \sqrt{\xi}}\mathbf{u}(\mathbf{r}_R) \quad (2)$$

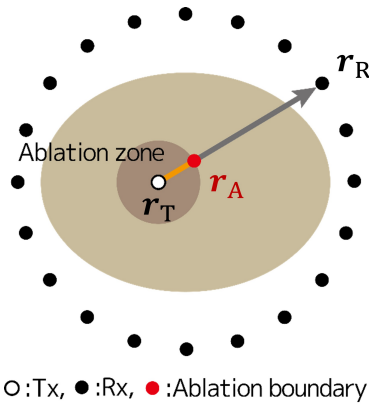


Fig. 2: Conceptual figure in the TDOA based ablation zone boundary estimation. The straight line propagation from the source r_T to the receiver r_R via the ablation boundary point r_A is assumed.

where $\mathbf{u}(r_R)$ is the unit vector pointing from r_T to r_R . Note that $\Delta\tau$ can be determined by identifying the peak shift in the following cross-correlation function:

$$\Delta\tau(r_R) = \arg \max_{\tau} [e_{\text{pre}}^T(t; r_T, r_R) \star e_{\text{dur}}^T(t; r_T, r_R)](\tau), \quad (3)$$

where \star is the cross-correlation operator, and is defined as

$$f(t) \star g(t) \equiv \int_{-\infty}^{\infty} f^*(\tau)g(t + \tau)d\tau, \quad (4)$$

where $*$ denotes the complex conjugate [23]. Finally, the ablation zone $\Omega_{\text{ab}}(\xi)$ is defined as the inner region enclosed by numerous boundary points as $r_A(r_R)$. Notably, this method requires a prior knowledge of ξ , which is related to the temperature variations in the vicinity of the MWA probe, but it cannot directly be obtained from microwave-based measurements only.

C. TDOA Prior CSI

To overcome the challenges outlined in Sec. II-B, in this study, we combine the TDOA boundary estimation with a CSI-based quantitative reconstruction framework. CSI is a promising non-linear inverse scattering approach because it avoids the iterative use of the forward solver, such as the FDTD solver, and it accelerates the optimization process of the quantitative reconstruction in the ablation zone. However, in the context of ablation monitoring, CSI also suffers from ill-posedness and non-linearity. To overcome these challenges, this study introduces a TDOA-prior CSI approach, where the ablation zone $\Omega_{\text{ab}}(\xi)$ and the temporal change in complex permittivity are simultaneously determined through CSI optimization. Here, the scattered field during the ablation state, $E_{\text{dur}}^S(\omega; r_T, r_R)$, is formulated by the following domain integral equation (DIE) as:

$$\begin{aligned} E_{\text{dur}}^S(\omega; r_T, r_R) &\equiv E_{\text{dur}}^T(\omega; r_T, r_R) - E^I(\omega; r_T, r_R) \\ &= k_B^2 \int_{\Omega_D} G_B(\omega; r, r_R) \mathcal{W}(\omega; r_T, r, \xi) dr \end{aligned} \quad (5)$$

where $E_{\text{dur}}^T(\omega; r_T, r_R)$ is the frequency domain expression of $e_{\text{dur}}^T(t; r_T, r_R)$. k_B and $G_B(\omega; r, r_R)$ express the wave-number and the Green's function of the background medium, assuming a vacuum, respectively. $\mathcal{W}(\omega; r_T, r, \xi) \equiv \chi(r; \xi) E_{\text{dur}}^T(\omega; r_T, r)$ is defined as the contrast source, where $\xi \equiv (\xi_1, \xi_2)$ is the newly introduced vector parameter. Although both ξ_1 and ξ_2 are defined as the ratios of the relative permittivity obtained from the pre-ablation and during the ablation stages, as defined in ξ , they are independent variables that determine the ablation boundary and the change in complex permittivity in the following algorithm. Using the prior estimate of the ablation boundary as $\Omega_{\text{ab}}(\xi)$ obtained from the TDOA approach, $\chi(r; \xi) \equiv (\epsilon_{\text{dur}}(\omega; r, \xi) - \epsilon_B(r))/\epsilon_B(r)$ is introduced where $\epsilon_B(r)$ is the background complex permittivity. Here, $\epsilon_{\text{dur}}(\omega; r; \xi)$ is determined as follows:

$$\epsilon_{\text{dur}}(\omega; r, \xi) \equiv \begin{cases} \xi_1 \epsilon_{\text{pre}}(\omega; r) & (r \in \Omega_{\text{ab}}(\xi_2)) \\ \epsilon_{\text{pre}}(\omega; r) & (r \in \bar{\Omega}_{\text{ab}}(\xi_2) \cap \Omega_D) \end{cases} \quad (6)$$

where $\epsilon_{\text{pre}}(\omega; r)$ is the complex permittivity profile in the pre-ablation state, ξ_1 is the quantitative change in complex permittivity in the ablation zone, and $\Omega_{\text{ab}}(\xi_2)$ is the prior ablation zone, determined by the TDOA method in Sec. II-B, when $\xi = \xi_2$. $\bar{\Omega}_{\text{ab}}(\xi_2)$ denotes the complementary set of $\Omega_{\text{ab}}(\xi_2)$. Notably, the variables ξ_1 and ξ_2 are treated as independent in the subsequent optimization scheme, because the ablation zone $\Omega_{\text{ab}}(\xi_2)$ may contain errors even with an accurate estimate of ξ_1 .

Thus, the proposed approach introduces a modified cost function in the CSI, taking into account the data and state equations as:

$$\begin{aligned} F(\mathcal{W}; \omega, \xi) &\equiv \frac{\sum_{r_T} \|E_{\text{dur}}^S(\omega; r_T, r_R) - \mathcal{G}^S[\mathcal{W}]\|_{\Omega_S}^2}{\sum_{r_T} \|E_{\text{dur}}^S(\omega; r_T, r_R)\|_{\Omega_S}^2} \\ + \lambda \frac{\sum_{r_T} \|\mathcal{W}(\omega; r_T, r, \xi) - \chi(r, \xi) (E^I(\omega; r_T, r') + \mathcal{G}^D[\mathcal{W}])\|_{\Omega_D}^2}{\sum_{r_T} \|\chi(r, \xi) E^I(\omega; r_T, r')\|_{\Omega_D}^2}, \end{aligned} \quad (7)$$

where λ is the regularization coefficient, and the operators \mathcal{G}^S and \mathcal{G}^D are defined as:

$$\begin{aligned} \mathcal{G}^S[\mathcal{W}] &= k_B^2 \int_{\Omega_D} G_B(\omega; r_R, r) \mathcal{W}(\omega; r_T, r, \xi) dr, \\ & (r_R \in \Omega_S), \end{aligned} \quad (8)$$

$$\begin{aligned} \mathcal{G}^D[\mathcal{W}] &= k_B^2 \int_{\Omega_D} G_B(\omega; r', r) \mathcal{W}(\omega; r_T, r, \xi) dr, \\ & (r' \in \Omega_D), \end{aligned} \quad (9)$$

$\|\cdot\|_{\Omega_S}^2$ and $\|\cdot\|_{\Omega_D}^2$ express the l_2 norms calculated in Ω_S and Ω_D , respectively.

Finally, the optimal $\hat{\xi}$ is determined as follows:

$$\hat{\xi} = \arg \min_{\xi} \left(\sum_{\omega \in \omega_{\text{all}}} \min_{\mathcal{W}} F(\mathcal{W}; \omega, \xi) \right) \quad (10)$$

Notably, when minimizing $F(\mathcal{W}; \omega, \xi)$, only the variable $E_{\text{dur}}^T(\omega; r_T, r)$ included in $\mathcal{W}(\omega; r_T, r, \xi)$, is updated, where $\chi(r, \xi)$ is fixed in Eq. (7). Figure 3 shows a schematic

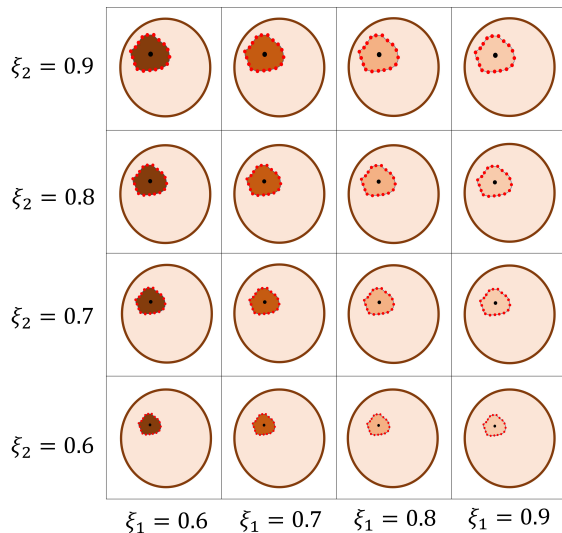


Fig. 3: Schematic illustration of the proposed method in optimizing the parameters for ablation boundary ξ_2 and dielectric property change ξ_1 . Red dots denote the ablation boundary points estimated by the TDOA method.

illustration of the proposed method, where the possible combinations of (ξ_1, ξ_2) are investigated to determine an appropriate vector parameter $\xi \equiv (\xi_1, \xi_2)$ as to the complex permittivity change (ξ_1) and the ablation boundary estimation (ξ_2) via minimizing the CSI cost function in Eq. (10).

D. Procedure

The processing flow of our proposed method is summarized as follows:

- Step 1) The scattered signals are recorded at the pre-ablation and during ablation states, denoted as $e_{\text{pre}}^T(t; \mathbf{r}_T, \mathbf{r}_R)$ and $e_{\text{dur}}^T(t; \mathbf{r}_T, \mathbf{r}_R)$, respectively.
- Step 2) For a given ξ , the complex permittivity profile during ablation, which is represented as $\epsilon_{\text{dur}}(\omega; \mathbf{r}, \xi)$, and the ablation area $\Omega_{\text{ab}}(\xi_2)$, are determined using the TDOA scheme through Eq. (2).
- Step 3) The CSI cost function is minimized with respect to the variable \mathcal{W} for $F(\mathcal{W}; \omega, \xi)$ in Eq. (7), and the optimized parameters $\hat{\xi}$ are obtained.
- Step 4) Using $\hat{\xi}$, the complex permittivity profile $\epsilon_{\text{dur}}(\omega; \mathbf{r}, \hat{\xi})$ and the ablation zone $\Omega_{\text{ab}}(\hat{\xi}_2)$ are determined.

Figure 4 shows the processing flow of the proposed method, representing the above process. This method has a distinct advantage because it simultaneously and independently optimizes both the ablation zone boundary $\Omega_{\text{ab}}(\hat{\xi}_2)$ and the change in dielectric properties $\epsilon_{\text{dur}}(\omega; \mathbf{r}, \hat{\xi})$.

Some theoretical bases that support the relevance of the proposed method are summarized as follows.

- 1) The first theoretical point is supported by the DIE in Eq. (5)), which also derives the cost function for the CSI, in Eq. (7). If we provide the ground truth profile of the ablation boundary and the dielectric profile, *i.e.*,

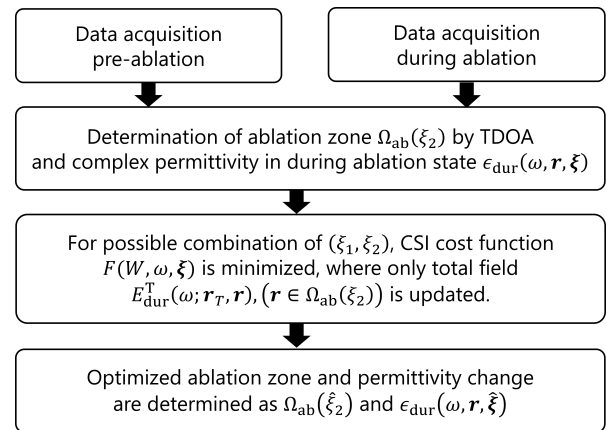


Fig. 4: Procedure of the proposed algorithm.

χ , \mathcal{W} , or $E_{\text{dur}}^T(\omega; \mathbf{r}_T, \mathbf{r})$, Eq. (5) is rigorously satisfied in both areas Ω_S and Ω_D . Then, if we minimize the cost function of the CSI by choosing an appropriate ablation zone and its decrease in permittivity ξ , the reconstruction results must be close to the ground truth profile. This is an important theoretical basis that also supports the relevance of the procedure for the proposed method, *i.e.*, searching an optimal ablation zone (ξ_1) and a temporal change of the dielectric profile (ξ_2) to minimize the CSI cost function.

- 2) Second, if we consider a large number of inversion cells, including a whole part of the breast, the ill-posed condition may lead to a local optimal solution. Thus, the proposed scheme minimizes the cost function by focusing on only the total fields to reduce the number of unknowns. To achieve the above scheme, the proposed method introduces the updating schemes only for the parameters related to the total fields as \mathcal{W} and $E_{\text{dur}}^T(\omega; \mathbf{r}_T, \mathbf{r})$, where their corresponding contrast functions χ are not updated during minimization of the cost function in the CSI. Thus, by reducing the number of independent variables to only the total fields, the proposed scheme is able to further alleviate the ill-posed condition, which is also a theoretically established point, by solving the inverse problem with a limited number of data samples.
- 3) Furthermore, it is also theoretically established that a total search approach during the optimization process can avoid a local optimal solution. The proposed method introduces the total search scheme by investigating all the possible combinations of ξ_1 and ξ_2 , as described in Fig. 3.

Thus, it is expected that our proposed scheme will provide more accurate complex permittivity reconstruction compared to the original CSI, if the assumptions (*i.e.*, the dielectric profile in the ablation zone is uniformly changed and the prior knowledge of the dielectric profile at the pre-ablation state is completely provided) are satisfied.

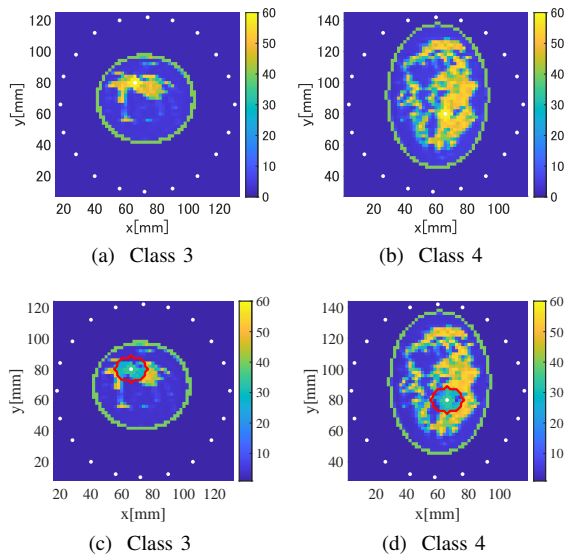


Fig. 5: The spatial profile of the real part of complex permittivity at 1.04 GHz in the MRI-derived 2-D numerical breast models of Class 3 and 4 at the case of $\xi = 0.6$. 1st row: Pre-ablation state. 2nd row: During-ablation state. White dots at external and internal area of breast denote the receiver and transmitter positions, respectively. Red closed curve in (c) and (d) denotes the boundary of the ablation zone.

III. RESULTS: NUMERICAL TEST

A. Numerical Setting

The 2D FDTD method, which is the most accurate method employed in full-wave electromagnetic simulators, is used to generate the scattered data in the MWA model, where the frequency-dependent property of each tissue, which is represented as a single-pole Debye model, is implemented using the in-house codes of the University of Wisconsin–Madison. The evaluation uses two MRI-derived realistic numerical phantoms of healthy women from an online database [24], [28]: a Class-3 “heterogeneously dense” phantom (ID number 062204) and a Class-4 “very dense” phantom (ID number 012304). The frequency-dependent dielectric properties of each breast tissue are modeled using single-pole Debye models as $\bar{\epsilon}(\omega) = \epsilon_\infty + \frac{\epsilon_s - \epsilon_\infty}{1 + j\omega\tau_0} + \frac{\sigma}{j\omega\epsilon_0}$ over the frequency range from 0.1 to 3.5 GHz, as described in [29]. The transmitted source current generates a Gaussian-modulated pulse with a center frequency of 2.45 GHz and a 3 dB bandwidth of 1.9 GHz. Both the cell size in the FDTD and the CSI in the computational domain are set to 2.0 mm. Fig. 5 shows the spatial profiles of the real part of complex permittivity at 1.04 GHz in each class for pre-ablation and during-ablation states, where the interstitial point source is placed in the cancerous tissue area (indicated by a white solid circle). The 20 receivers are arranged in a circular pattern around the external area of the breast. For this study, it is assumed that the spatial profiles of the three Debye parameters ϵ_∞ , $\Delta\epsilon$, and σ are provided only for the pre-ablation state. This assumption is not necessarily impractical because pre-surgical MRI or CT scans can be performed, and these images

can be linked to dielectric properties using online databases such as [32]. Additionally, we assume that the ablation boundary has an ellipsoidal shape featuring a 2-mm-radius cancerous tissue at the center; this is based on numerous studies [25]–[27], which demonstrated that the ablation zone typically forms an ellipsoidal cross-section affected by factors such as the heterogeneity of breast tissue and the beam pattern of the ablation probe. The Debye parameters for this tissue are defined as $(\epsilon_\infty, \Delta\epsilon, \sigma) = (58.0, 20.0, 0.8 \text{ S/m})$, which are approximately 1.2 times larger than those of fibroglandular tissue. Furthermore, in the ablation zone, these Debye parameters uniformly decrease, indicating that the spatial profiles inside and outside the ablation zone are not homogeneous. Note that, in the optimization process in the CSI or other scheme, we focus on the single frequency sample at 1.04 GHz in all the results.

B. Reconstruction Results in Different Classes and Drop Rates

First, we assess the reconstruction performance across different classes and drop rates ξ , with three specific drop rates set at 0.6, 0.7, and 0.8 for all Debye parameters in the ablation zone. These drop rates correspond to temperatures of 90°C, 93°C, and 95°C, as demonstrated in bovine liver ablation experiments [10]. To compare methods, we also evaluate the reconstruction performance of the original CSI, using the entire breast media as the ROI. Notably, for a fair comparison, prior knowledge of the true Debye profiles at the pre-ablation state is also provided in the original CSI, though the impact of ablation ξ is not included. Furthermore, in evaluating the proposed method, two different conditions are examined. The first condition involves calculating the total fields in the breast media, denoted as $E_{\text{dur}}^T(\omega; \mathbf{r}_T, \mathbf{r}_R)$, using the FDTD method. In this case, there are no errors in estimating the total fields when calculating the cost function $F(\mathcal{W}; \omega, \xi)$. The second condition involves estimating $E_{\text{dur}}^T(\omega; \mathbf{r}_T, \mathbf{r}_R)$ by minimizing the CSI cost function as described in Eq. (7) in Sec. II-C. Notably, either the first or the second condition employs the proposed scheme described in Sec. II-D, except for generating the total field for evaluating the cost function described in Eq. (7), *i.e.*, in the Step 3). Figs. 6, 7, and 8 depict the reconstruction results for each class with drop rates for both the real and imaginary parts of the complex permittivity in the cases of $\xi = 0.6$, $\xi = 0.7$, and $\xi = 0.8$ cases, respectively, where the original CSI method is compared with the proposed approach under the above two conditions. In the CSI scheme, the number of iterations for updating the cost function is set to 500 in all cases. The results from the original CSI scheme reveal considerable inaccuracies inside and outside the ablation zone across all classes and ξ . Here, in the original CSI scheme, the contrast source \mathcal{W} , which is used to calculate the cost function described in Eq. (7), including $\mathcal{G}^S[\mathcal{W}]$ and $\mathcal{G}^I[\mathcal{W}]$, is initially provided by the back propagation (BP) algorithm; \mathcal{W} is sequentially updated using conjugate gradient optimization scheme, which is commonly used optimization scheme [20]. This issue primarily arises

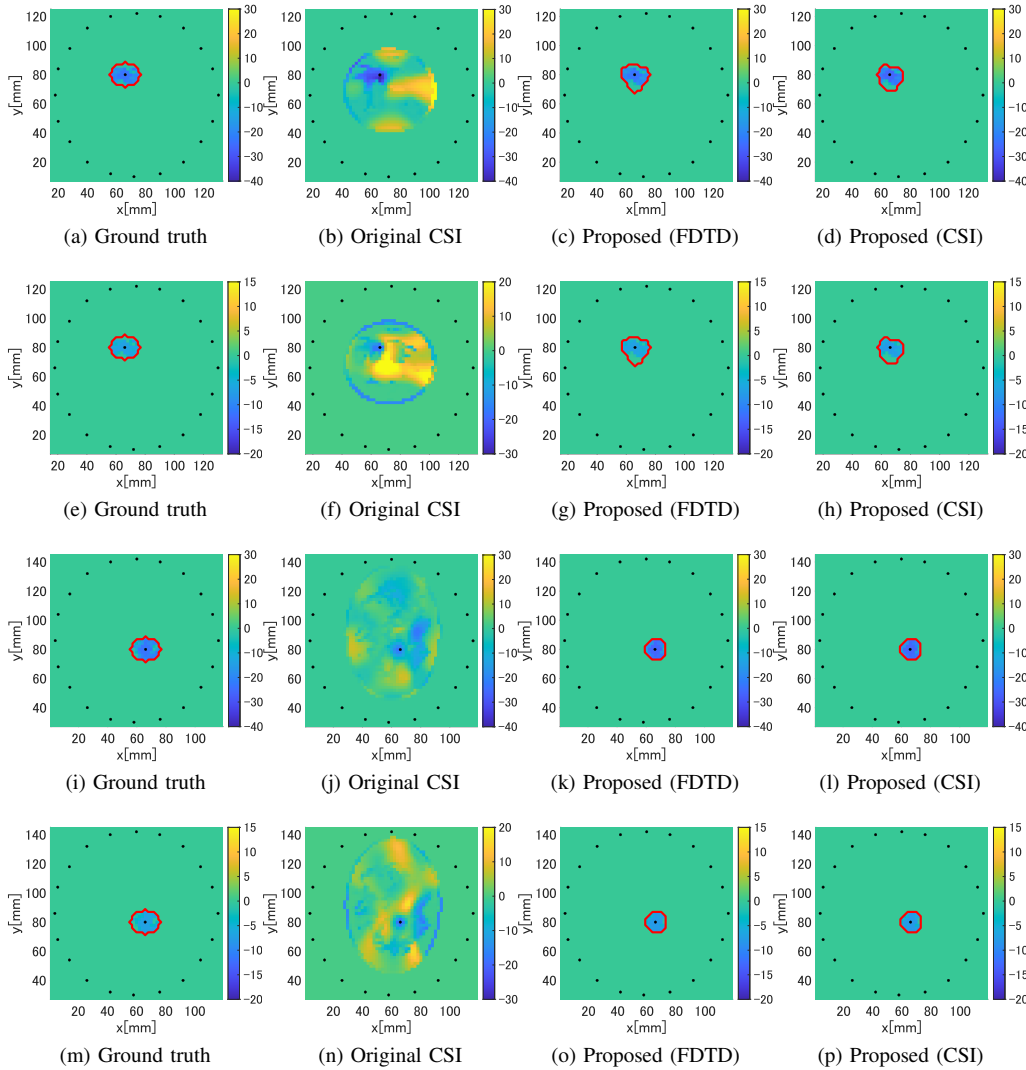


Fig. 6: Reconstruction differential profiles between pre- and during ablation states ($\xi = 0.6$). 1st and 2nd rows: Real and Imaginary parts in Class 3, respectively. 3rd and 4th rows: Real and Imaginary parts in Class 4, respectively.

from ill-posed conditions, where the number of unknown cells used in optimizing the total fields is assumed to be 728 and 1220 for Class 3 and Class 4, respectively, while the number of data points is 20. Although the original CSI method can identify the decreasing dielectric property in the ablation zone, it tends to overestimate the properties both inside and outside the ablation area. In contrast, the proposed scheme provides a more accurate reconstruction of the ablation boundary and the changes in dielectric properties by simultaneously optimizing ξ_1 , the drop rates in the ablation zone, and ξ_2 which determines the TDOA-based ablation boundary. This is because, in the proposed scheme, the total fields in the breast media are only updated, while the contrast function χ is kept fixed when minimizing the cost function described in Eq. 7. For example, the numbers of unknowns counted in the true ROI in Classes 3 and 4 are both 63, whereas the original CSI requires 728 and 1,220 unknowns in Class 3 and 4, respectively; this is because it assumes

the entire breast as Ω_D , showing that the proposed approach significantly mitigates the ill-posed condition. Notably, when comparing results from FDTD and CSI-based total field calculations (shown in (e,f) and (g,h)), there are only slight differences owing to reconstruction errors inherent in the CSI-based optimization. However, there is no considerable degradation in the reconstruction accuracy even with CSI-based optimization, which justifies the use of the CSI method in optimizing the cost function of $F(\mathcal{W}; \omega, \xi)$, instead of using the FDTD method. This indicates that the proposed scheme can achieve a certain level of accuracy of the total field reconstruction by alleviating ill-posed conditions.

To provide a quantitative error analysis, we introduce two error indices for assessing changes in dielectric properties and ablation zone estimation. First, the root mean square error (RMSE) for the quantitative reconstruction of the real part

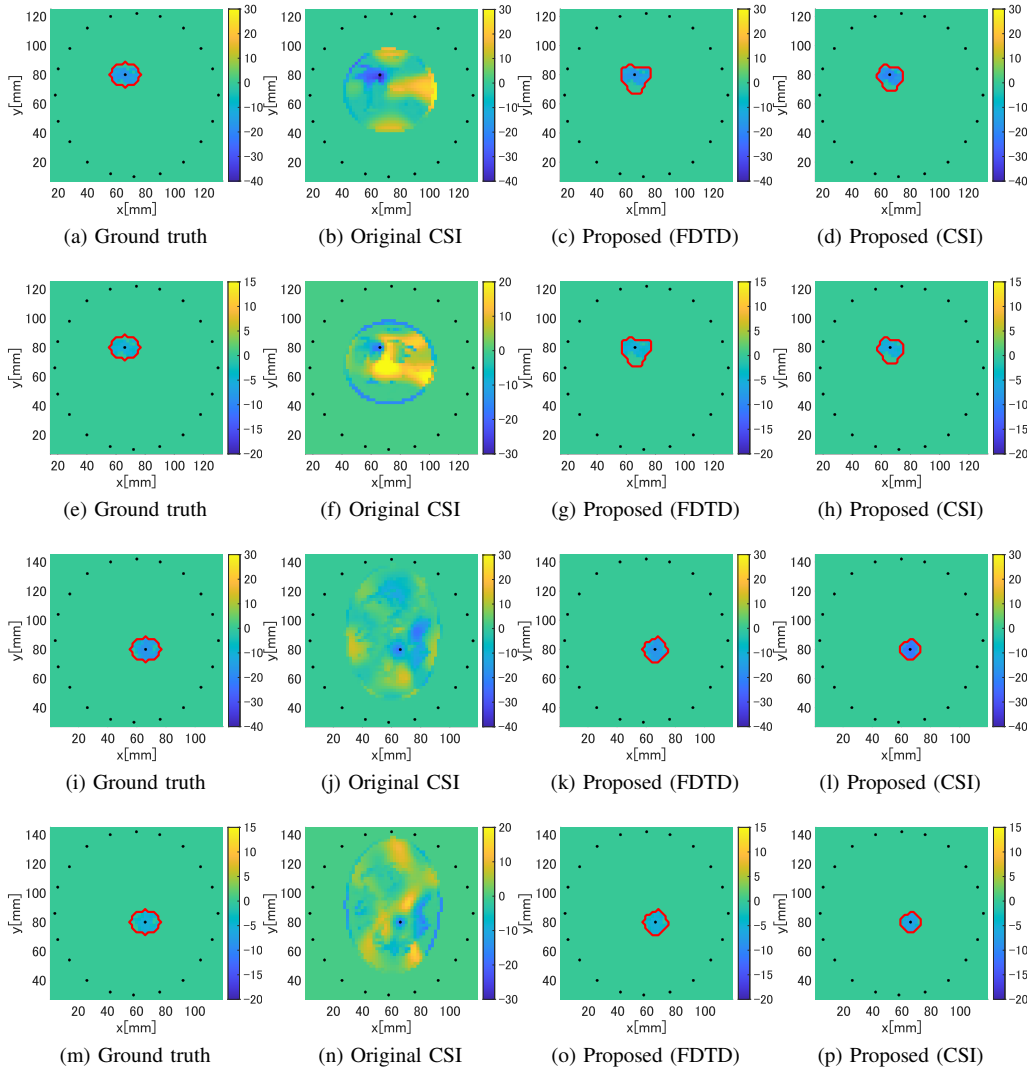


Fig. 7: Reconstruction differential profiles between pre- and during ablation states ($\xi = 0.7$). 1st and 2nd rows: Real and Imaginary parts in Class 3, respectively. 3rd and 4th rows: Real and Imaginary parts in Class 4, respectively.

TABLE I: RMSE of the real part of complex permittivity at 1.04 GHz in each case.

	Class 3			Class 4		
	Original	Proposed (FDTD)	Proposed (CSI)	Original	Proposed (FDTD)	Proposed (CSI)
$\xi = 0.6$	10.65	1.23	2.00	6.07	2.02	2.02
$\xi = 0.7$	9.96	1.19	1.50	6.05	1.45	1.94
$\xi = 0.8$	10.88	1.16	1.50	6.28	0.98	1.61

of the complex permittivity is defined as

$$\text{RMSE} = \sqrt{\frac{\int_{\mathbf{r} \in \Omega_D} |\Re[\epsilon_{\text{dur}}^{\text{true}}(\mathbf{r})] - \Re[\epsilon_{\text{dur}}^{\text{est}}(\mathbf{r})]|^2 d\mathbf{r}}{\int_{\mathbf{r} \in \Omega_D} d\mathbf{r}}}, \quad (11)$$

In addition, the spatial mismatch between true and reconstruction ablation zones is defined as $\text{Err}_{\Omega_{\text{ab}}}$:

$$\text{Err}_{\Omega_{\text{ab}}} = \frac{\int_{\mathbf{r} \in \Omega_D} |\eta_{\text{true}}(\mathbf{r}) - \eta_{\text{est}}(\mathbf{r})| d\mathbf{r}}{\int_{\mathbf{r} \in \Omega_D} |\eta_{\text{true}}(\mathbf{r})| d\mathbf{r}}. \quad (12)$$

Here $\eta_{\text{true}}(\mathbf{r})$ and $\eta_{\text{est}}(\mathbf{r})$ are defined as:

$$\eta_{\text{true}}(\mathbf{r}) \equiv \begin{cases} 1 & (\mathbf{r} \in \Omega_{\text{ab}}^{\text{true}}) \\ 0 & (\text{Otherwise}) \end{cases} \quad (13)$$

$$\eta_{\text{est}}(\mathbf{r}) \equiv \begin{cases} 1 & (\mathbf{r} \in \hat{\Omega}_{\text{ab}}) \\ 0 & (\text{Otherwise}) \end{cases} \quad (14)$$

where $\Omega_{\text{ab}}^{\text{true}}$ and $\hat{\Omega}_{\text{ab}}$ are the true and estimated ablation zone areas, respectively. Tables I, II and III present the RMSEs of the real and imaginary parts of the complex permittivity and $\text{Err}_{\Omega_{\text{ab}}}$ for each method. As shown in Tables I and II, the

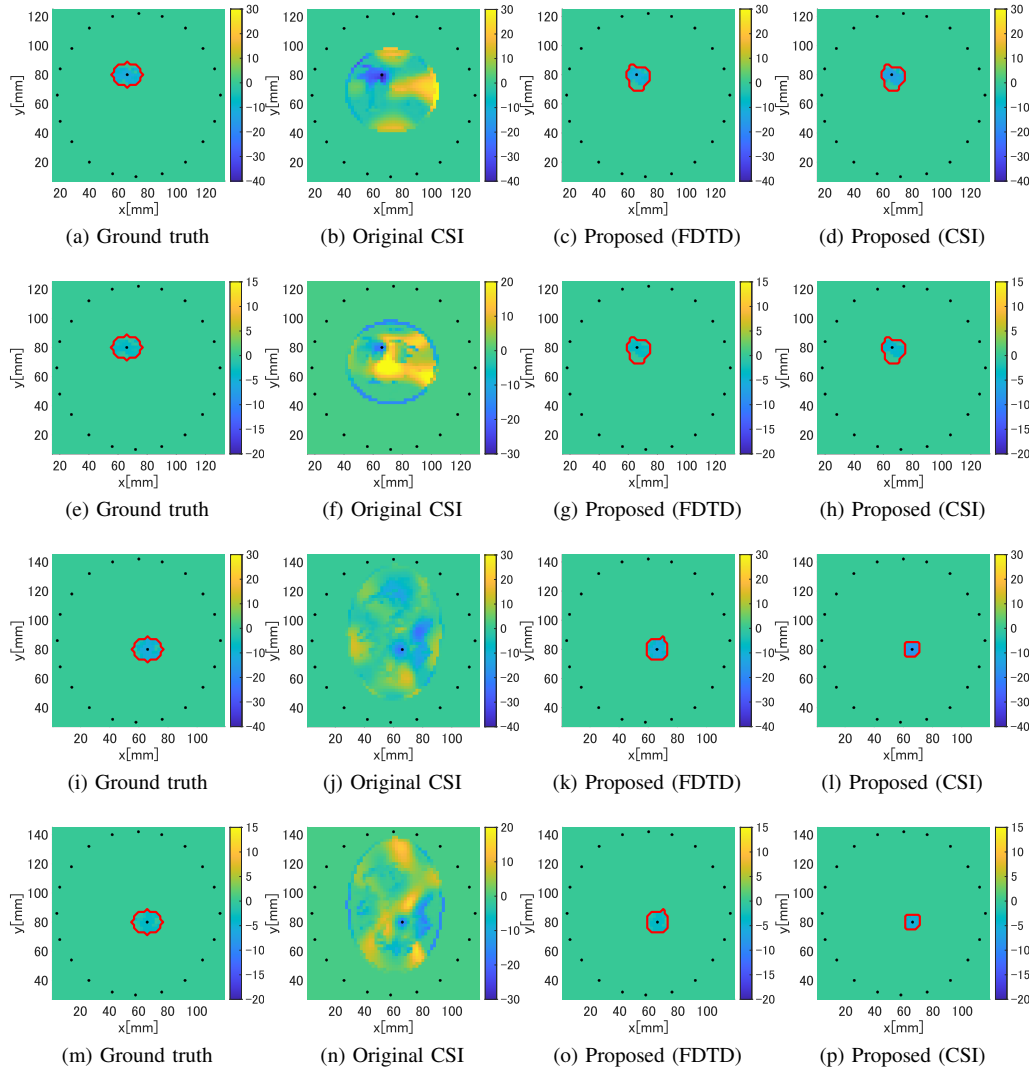


Fig. 8: Reconstruction differential profiles between pre- and during ablation states ($\xi = 0.8$). 1st and 2nd rows: Real and Imaginary parts in Class 3, respectively. 3rd and 4th rows: Real and Imaginary parts in Class 4, respectively.

TABLE II: RMSE of the imaginary part of complex permittivity at 1.04 GHz in each case.

	Class 3			Class 4		
	Original	Proposed (FDTD)	Proposed (CSI)	Original	Proposed (FDTD)	Proposed (CSI)
$\xi = 0.6$	10.34	0.38	0.63	5.87	0.64	0.64
$\xi = 0.7$	10.03	0.37	0.46	5.45	0.47	0.61
$\xi = 0.8$	10.08	0.36	0.40	5.93	0.31	0.51

RMSE of both the real and imaginary parts in the original CSI method are considerably larger than those obtained using the proposed method under both conditions, when using the FDTD and CSI for the total field calculation. Notably, since the parameter ξ determines the same dropping rate for the real and imaginary parts in the proposed method as defined by $\xi \equiv \bar{\epsilon}_{dur}/\bar{\epsilon}_{pre}$, the reconstruction profiles of the real and imaginary parts are linearly associated. Moreover, the RMSEs for the proposed method are similar regardless of whether using FDTD or CSI-based total field optimization,

which demonstrates the reliability of CSI for generating total fields. Furthermore, regarding the ablation zone boundary estimation, differences are observed between the FDTD and CSI calculations, particularly for the Class 4 model and higher ξ values. This discrepancy arises because the Class 4 model, which includes a higher proportion of fibro-glandular tissues compared to Class 3, introduces non-linear effects that can affect the accuracy of total field optimization.

TABLE III: Estimation error of the ablation zone estimate as $\text{Err}_{\Omega_{ab}}$ in the proposed method in each case.

	Class 3		Class 4	
	Proposed (FDTD)	Proposed (CSI)	Proposed (FDTD)	Proposed (CSI)
$\xi = 0.6$	0.10	0.20	0.33	0.33
$\xi = 0.7$	0.14	0.19	0.23	0.40
$\xi = 0.8$	0.26	0.26	0.27	0.59

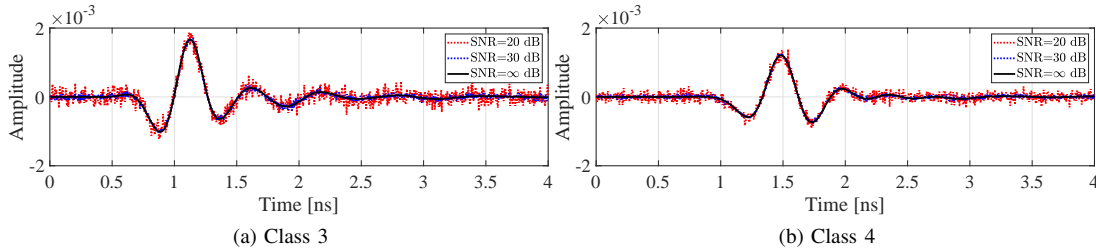


Fig. 9: Example of scattered signals in each SNR level in Class 3 and 4 models. Black solid : SNR = ∞ . Blue broken : SNR = 30 dB. Red broken : SNR = 20 dB.

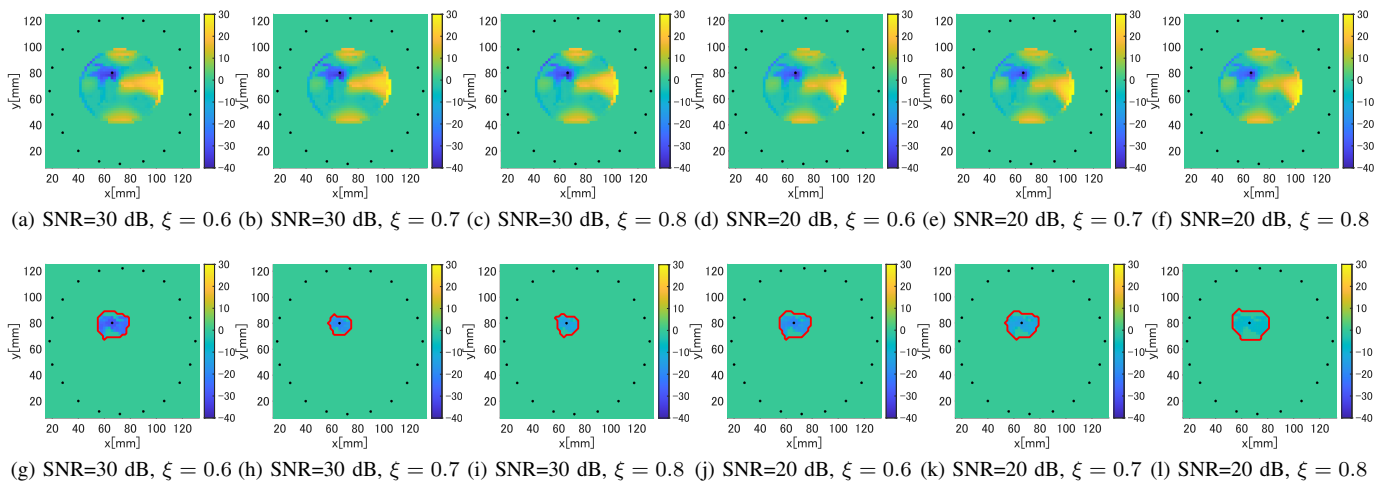


Fig. 10: Reconstruction differential profiles between pre- and during ablation states in the real part of the complex permittivity at 1.04 GHz at each SNR level and ξ in Class 3. 1st row: Original CSI. 2nd row: Proposed method (CSI).

C. Sensitivity to Additive Noise

This section examines the sensitivity of each method to additive white noise, focusing on quantitative reconstruction performance. White Gaussian noise is added to each total field $e_{\text{pre}}^T(t; \mathbf{r}_T, \mathbf{r}_R)$ and $e_{\text{dur}}^T(t; \mathbf{r}_T, \mathbf{r}_R)$. The signal-to-noise ratio (SNR) is defined as the ratio of the maximum power of the scattered signals to the power of the noise in the time domain. We investigate two SNR scenarios: 30 and 20 dB. In the proposed method, CSI-based total field optimizations are applied to all results. Fig. 9 shows the examples of the scattered signals for different SNR levels; particularly, in the SNR = 20 dB case, the scattered signal suffers from noise data, which are expected to affect the TDOA and CSI reconstruction results. Figs. 10 and 11 show the reconstruction results for the original CSI and the proposed

TABLE IV: RMSE of the real part of complex permittivity at 1.04 GHz in Class 3 at each SNR level.

	Original		Proposed	
	30 dB	20 dB	30 dB	20 dB
$\xi = 0.6$	10.38	10.35	1.84	2.73
$\xi = 0.7$	10.68	10.21	1.60	2.05
$\xi = 0.8$	11.01	10.45	1.19	1.57

method at each SNR level and ξ for Class 3 and Class 4 cases.

Focusing on the results from the original CSI, considerable differences are not observed across various SNR and ξ levels. This is because the accuracy in the original CSI is mainly

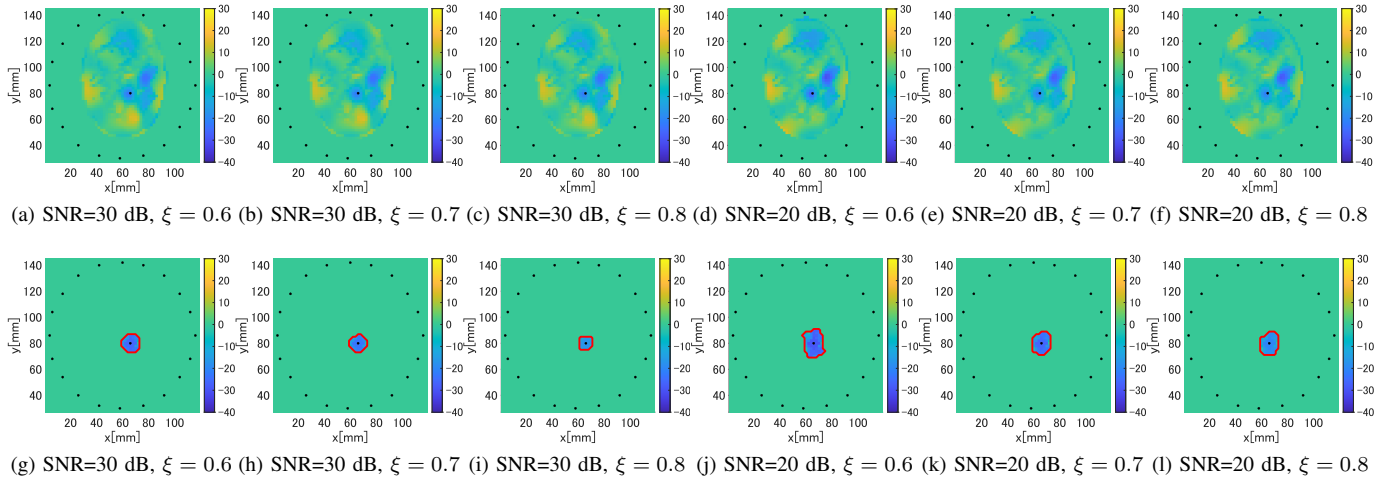


Fig. 11: Reconstruction differential profiles between pre- and during ablation states in the real part of the complex permittivity at 1.04 GHz at each SNR level and ξ in Class 4. 1st row: Original CSI. 2nd row: Proposed method (CSI).

TABLE V: RMSE of the real part of complex permittivity at 1.04 GHz in Class 4 at each SNR level.

	Original		Proposed	
	30 dB	20 dB	30 dB	20 dB
$\xi = 0.6$	6.37	7.18	3.61	3.25
$\xi = 0.7$	6.12	6.42	2.32	2.24
$\xi = 0.8$	6.25	6.58	2.86	2.00

TABLE VI: Estimation error of ablation zone estimate as $\text{Err}_{\Omega_{\text{ab}}}$ by the proposed method at each SNR level.

	Class 3		Class 4	
	30 dB	20 dB	30 dB	20 dB
$\xi = 0.6$	0.12	0.29	0.13	0.26
$\xi = 0.7$	0.22	0.32	0.30	0.25
$\xi = 0.8$	0.21	0.57	0.77	0.26

determined by severe ill-posed conditions not so much by the SNR level. In contrast, while there are some differences among SNR levels in the ablation zone and complex permittivity change, it can offer accurate dielectric change profiles and ablation zone boundaries under both SNR scenarios. The robustness of the proposed method to noise can be attributed to several factors. One main reason is that the TDOA scheme employs cross-correlation processing for estimating TDOA, as described in Eq. (3), corresponding to the matched filter, which is an efficient noise reduction technique [30], [31]. Consequently, TDOA boundary estimation is less sensitive to additive noise, as demonstrated in [19]. Another reason for the proposed method's robustness is that the CSI uses frequency data. Focusing on the frequency samples near the center frequency (where the magnitude are the highest), the SNR can be improved compared with that corresponding to frequency samples with lower magnitudes. Tables IV and V summarize the RMSE of the reconstruction results for the real part of the complex permittivity in Class 3 and Class 4. These tables quantitatively demonstrate that our proposed method is highly resilient to additive noise in terms of quantitative reconstruction performance. Furthermore, Table VI presents the errors in ablation boundary estimation, denoted as $\text{Err}_{\Omega_{\text{ab}}}$. Although considerable errors are observed in the case of $\xi = 0.8$ owing to random noise effects and inherent boundary estimation errors from the TDOA process, these values are

generally below 0.3. This indicates that the relative errors in ablation zone estimation are within 30 %.

D. Sensitivity to Prior Knowledge Error

An important assumption in the proposed method and the original CSI is that the Debye parameter profiles in the pre-ablation state are accurately known. Although this assumption is generally reasonable, these profiles may contain some errors when estimated from MRI or CT-based profiles. Therefore, this section investigates the sensitivity of the method to errors in the Debye parameters in the pre-ablation state. To simulate this scenario, Gaussian random noise is added to the true pre-ablation profiles for all three Debye parameters ϵ_{∞} , $\Delta\epsilon$, and σ . The standard deviations for each parameter as $\sigma_{\epsilon_{\infty}}^{\text{pre}}$, $\sigma_{\Delta\epsilon}^{\text{pre}}$, and $\sigma_{\sigma}^{\text{pre}}$ are defined as:

$$\sigma_{\epsilon_{\infty}}^{\text{pre}} = \alpha \max_{\mathbf{r}} \epsilon_{\infty}^{\text{pre}}(\mathbf{r}) \quad (15)$$

$$\sigma_{\Delta\epsilon}^{\text{pre}} = \alpha \max_{\mathbf{r}} \Delta\epsilon^{\text{pre}}(\mathbf{r}) \quad (16)$$

$$\sigma_{\sigma}^{\text{pre}} = \alpha \max_{\mathbf{r}} \sigma^{\text{pre}}(\mathbf{r}) \quad (17)$$

where $\epsilon_{\infty}^{\text{pre}}(\mathbf{r})$, $\Delta\epsilon^{\text{pre}}(\mathbf{r})$, and $\sigma^{\text{pre}}(\mathbf{r})$ are the true Debye parameters in the pre-ablation state. The constant α is the error level. We investigate two different values for α i.e., 0.05 and 0.1, as illustrated in Figs. 12 and 13, respectively. When comparing these results to those without errors in the pre-ablation state, as shown in Figs. 6 (d), (h), Fig. 7 (d), (h),

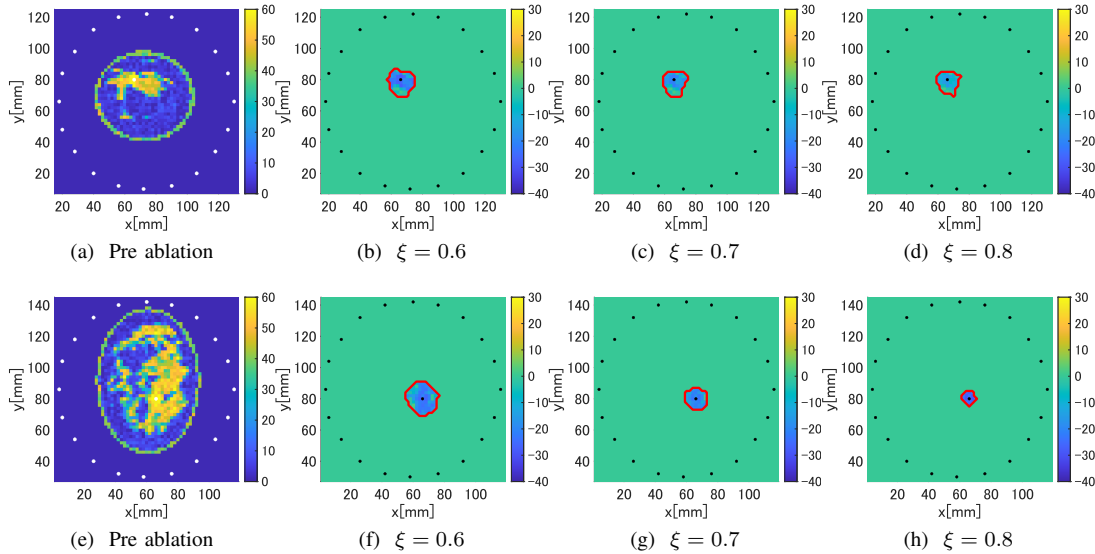


Fig. 12: Reconstruction differential profiles of the real part of the complex permittivity at 1.04 GHz, in the case that the Debye parameters of pre-ablation states includes errors, in using the proposed method (CSI). Standard deviation of Gaussian noise is 5 % ($\alpha = 0.05$) of each maximum Debye parameter. 1st row: Class 3. 2nd row: Class 4.

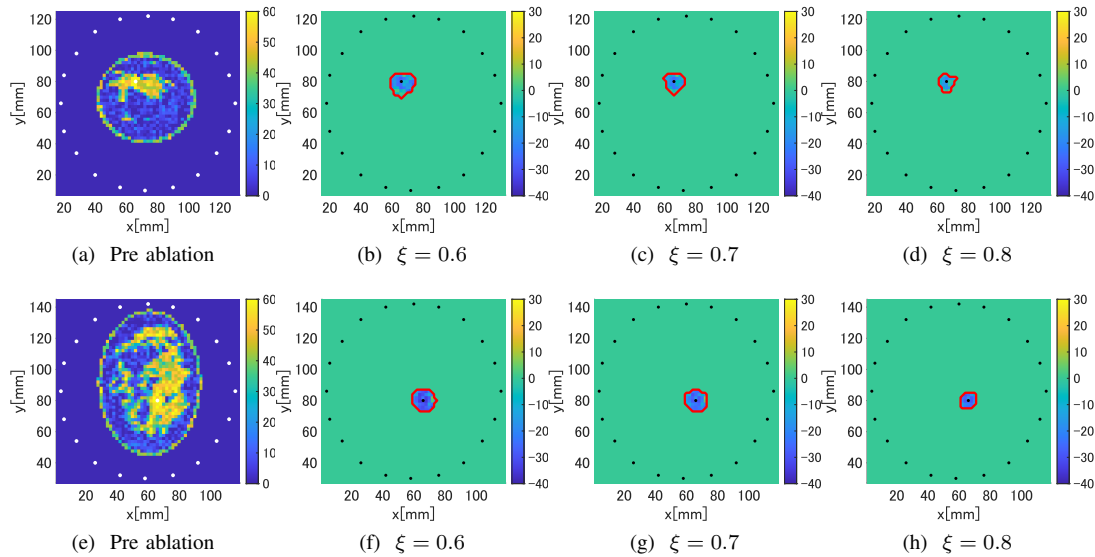


Fig. 13: Reconstruction differential profiles of the real part of the complex permittivity at 1.04 GHz, in the case that the Debye parameters of pre-ablation states includes errors, in using the proposed method (CSI). Standard deviation of Gaussian noise is 10 % ($\alpha = 0.1$) of each maximum Debye parameter. 1st row: Class 3. 2nd row: Class 4.

and Fig. 8 (d), (h), there is no considerable degradation in accuracy, even for $\alpha = 0.1$ in both classes. These findings are reflected in the RMSE and $\text{Err}_{\Omega_{ab}}$ comparisons summarized as in Tables VII and VIII. This robustness confirms that our proposed method can effectively compensate for errors in the pre-ablation state to a certain extent. This is achieved by limiting the ROI using the TDOA method and minimizing the CSI cost function based on the actual scattered signals.

E. Dependency of Selected Frequency Samples

In all the results in Sec. III-B, III-C, and III-D, the CSI based complex permittivity estimation was conducted at the single frequency of 1.04 GHz, whereas the pulse modulated transmitting signal has a wide frequency band ranging from 0.1 GHz to 3.5 GHz, as described in Sec. III-A. We expect that the final results obtained using the proposed scheme will significantly depend on the selected frequency samples. To further investigate and discuss the above points, we examine several cases using different frequency samples. Figures 14

TABLE VII: RMSE of the real part of complex permittivity at 1.04 GHz and $\text{Err}_{\Omega_{ab}}$ when the pre-ablation profile includes random errors in Class 3 using the proposed method (CSI).

	RMSE of $\Re[\epsilon]$			$\text{Err}_{\Omega_{ab}}$		
	0 %	5 %	10 %	0 %	5 %	10 %
$\xi = 0.6$	2.00	2.00	2.35	0.20	0.20	0.29
$\xi = 0.7$	1.50	2.00	2.48	0.19	0.32	0.46
$\xi = 0.8$	1.29	1.52	1.87	0.26	0.37	0.60

TABLE VIII: RMSE of the real part of complex permittivity at 1.04 GHz and $\text{Err}_{\Omega_{ab}}$ when the pre-ablation profile includes random errors in Class 4 using the proposed method (CSI).

	RMSE $\Re[\epsilon]$			$\text{Err}_{\Omega_{ab}}$		
	0 %	5 %	10 %	0 %	5 %	10 %
$\xi = 0.6$	2.02	2.30	2.12	0.33	0.11	0.28
$\xi = 0.7$	1.94	1.59	1.76	0.40	0.32	0.32
$\xi = 0.8$	1.61	2.26	2.05	0.59	0.72	0.60

and 15 show the reconstruction results of the real part of the complex permittivity by the proposed method for the single frequency data at 0.46 GHz, 1.50 GHz, and 1.96 GHz, using the case of $\xi = 0.6$, $\xi = 0.7$, and $\xi = 0.8$ for the Class 3 and 4 models, respectively. Table IX also summarizes the RMSE of the real part of the complex permittivity. As shown in these figures and tables, there are not significant differences among the results in using different frequencies, especially in Class 3, however, there are some degradation of the accuracy in using the 2.0 GHz samples at Class 4 cases. This is because the wavelength corresponding to 2.0 GHz in the high-permittivity cancerous and fibroglandular tissues is less than 20 mm, which does not satisfy the 1/10 wavelength criterion of a 2.0-mm cell size used in the FDTD calculation. Notably, the reconstruction accuracy in the proposed method can be improved using multiple frequency data. However, increasing the number of frequency points, in general, leads to increased computational cost. Consequently, it is essential to achieve a balance between accuracy and computational efficiency when selecting single- or multifrequency samples.

F. Limitations and Further Discussions

This section describes the limitations and further discussions in future work of the proposed method, considering a practical scenario. At first, since the proposed method requires a global optimization scheme for possible combinations of ξ_1 and ξ_2 , to determine the ablation zone boundary and its complex permittivity change independently, it needs a relatively larger computational complexity to retain an optimal combination as $\hat{\xi}_1$ and $\hat{\xi}_2$. In particular, the actual computational time required in the proposed method is approximately 4900 s in using the FDTD total field calculation, and 637 s in using the CSI based optimization in Class 3, while the original CSI requires 27 s, where

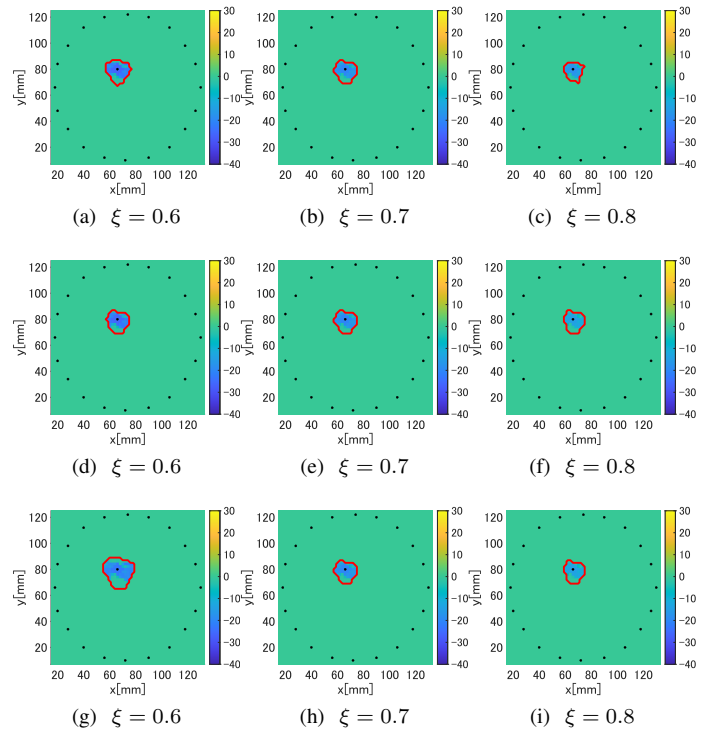


Fig. 14: Reconstruction differential profiles of the real part of the complex permittivity in Class 3 when using the different frequency samples. 1st row: Using 0.46 GHz data. 2nd row: Using 1.50 GHz data. 3rd row: Using 1.96 GHz data.

an Intel Xeon Silver 4210 CPU, 2.20 GHz, with 1028 GB RAM. The major part of the processing time in the proposed method is dominated in calculating (FDTD) or optimizing (CSI) the total field $E_{\text{dur}}^T(\omega; \mathbf{r}_T, \mathbf{r})$, for all combinations (49 combinations) of (ξ_1, ξ_2) with 500 iterations. Notably, in the proposed method, the CSI based optimization is approximately 7.7 times faster than that required in the FDTD calculation, demonstrating that the proposed scheme, using the CSI optimization, achieves a balance between the accuracy and computational efficiency, as described in Sec. III-B. However, in realistic scenario, the calculation time in the proposed method should be reduced to provide a quantitative image of ablation zone at the order of a minute in updating sequence. Thus, it is our important future task to accelerate the processing in optimizing total field, such as by exploiting the complex permittivity profile of the pre-ablation state, where an initial estimate of the total fields would be more appropriately provided by using a prior knowledge of pre-ablation state. Furthermore, by exploiting the reconstruction results in the previous snapshot in during the ablation, we can also narrow down the searching area of (ξ_1, ξ_2) around those obtained in the previous time-slot, which can significantly reduce the total calculation time in the reconstruction. Although this study is currently in a fundamental stage, it is not particularly challenging to reduce the overall computational time using the proposed scheme.

TABLE IX: RMSE of the real part of complex permittivity and $\text{Err}_{\Omega_{ab}}$ when the different frequency samples are used in the proposed method (CSI).

		RMSE of $\Re[\epsilon]$				$\text{Err}_{\Omega_{ab}}$			
		0.46 GHz	1.04 GHz	1.50 GHz	1.96 GHz	0.46 GHz	1.04 GHz	1.50 GHz	1.96 GHz
Class 3	$\xi = 0.6$	1.38	2.00	1.99	2.72	0.10	0.20	0.20	0.26
	$\xi = 0.7$	1.50	1.50	1.49	1.50	0.19	0.19	0.19	0.19
	$\xi = 0.8$	1.78	1.29	1.29	1.29	0.37	0.26	0.26	0.26
Class 4	$\xi = 0.6$	2.12	2.02	2.02	2.02	0.28	0.33	0.33	0.28
	$\xi = 0.7$	1.94	1.94	3.05	1.94	0.40	0.40	0.40	0.82
	$\xi = 0.8$	1.61	1.61	1.84	1.61	0.59	0.59	0.59	0.65

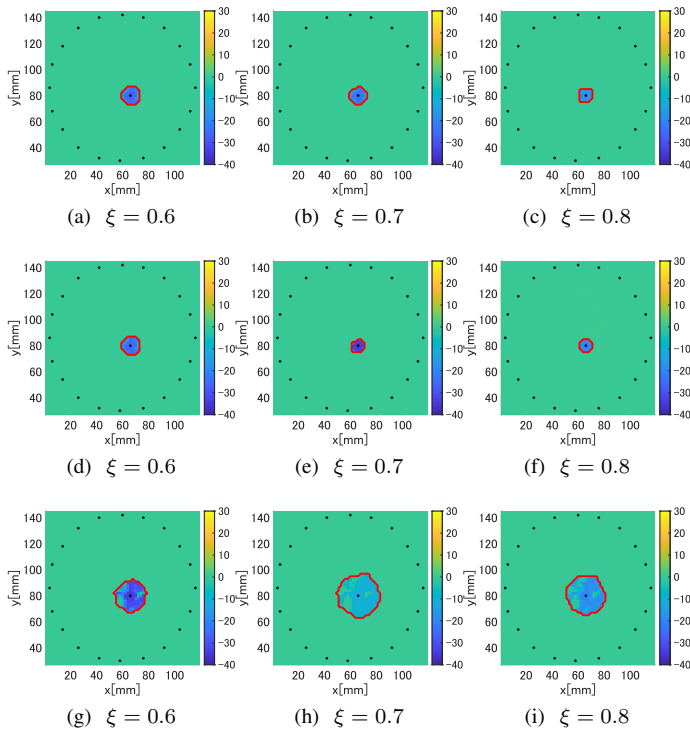


Fig. 15: Reconstruction differential profiles of the real part of the complex permittivity in Class 4 when using the different frequency samples. 1st row: Using 0.46 GHz data. 2nd row: Using 1.50 GHz data. 3rd row: Using 1.96 GHz data.

In addition, the reconstruction accuracy and the ablation zone boundary estimation significantly depend on the observation parameters, such as the number of receivers or the distance between the receivers and the MWA source. In this case described in Sec. III-A, the average distances from the transmitter to each receiver position in Classes 3 and 4 are 57.2 mm and 56.5 mm, respectively, and their corresponding standard deviations are 11.3 mm and 6.9 mm, respectively. The number of receivers affects both the TDOA ablation zone estimation and the CSI reconstruction performance: That is, it determines the number of sampling points required for TDOA boundary estimation, and if we obtain more receivers, it could contribute more accurate

boundary estimation, and vice versa. Additionally, in the CSI based dielectric profile reconstruction, the number of receivers affects the data volume, mitigating or exacerbating the ill-posed condition when optimizing the total fields to minimize the CSI cost function. Although a large number of receivers generally improves accuracy, there are practical limitations due to the physical size of the elements constituting the array and the complexity of the measurement modules. The distance between the transmitter (ablation center) and the receivers primarily affects the available SNR because as the distance increases, the propagation loss in the air also increases. In contrast, a short distance to the ablation probe is beneficial for the TDOA model, which assumes straight-line propagation without accounting for multiple scattering effects caused by the heterogeneity of the breast tissues. However, a short distance limits the number of receivers required because of the limited space available for the array structure. Considering the above, both the number of receivers and their distance from the transmitters must be carefully selected to optimize the reconstruction accuracy while considering the dimensional constraints of the array structure.

Furthermore, the proposed method requires some assumptions to guarantee reconstruction accuracy, such as that the dielectric profile in the ablation zone is uniformly changed and complete prior knowledge of the dielectric profile at the pre-ablation state is provided. If the above assumptions are not completely satisfied, the proposed method will suffer from some degradation in accuracy, and these factors determine the application range of the proposed method. However, it is expected that the proposed method can offer a significant advantage over the original CSI scheme by providing more accurate estimations for the ablation boundary and the change in complex permittivity by markedly reducing the number of unknowns. These points are also validated by the results in Sec. III-C or III-D, *e.g.*, the noisy case, including errors in the prior knowledge of the pre-ablation state.

IV. CONCLUSION

This study introduces a quantitative monitoring scheme for ablation zones by combining TDOA-based boundary estimation with CSI-based complex permittivity reconstruction for microwave-based MWA monitoring in breast cancer treatment. A key feature of the proposed method is its ability to simultaneously provide accurate and real-time boundary

estimation through TDOA imaging and to track the temporal changes in complex permittivity profiles by solving the non-linear inverse scattering problem with CSI. The use of TDOA to define a limited ROI helps mitigate the ill-posed conditions in the CSI reconstruction, allowing for more precise updates of the total fields according to different ablation impact scenarios. The 2-D numerical analysis using MRI-derived realistic phantoms demonstrates that our proposed method considerably improves reconstruction accuracy compared to the conventional CSI scheme. Additionally, sensitivity studies examining the effects of additive Gaussian noise and errors in the Debye profiles from pre-ablation states show that our method is resilient to these errors, ensuring its applicability in realistic scenarios. Ongoing research is focused on extending this approach to 3-D models and experimental validations.

REFERENCES

- [1] G. Carrafiello, D. Lagana, M. Mangini, F. Fontana, G. Dionigi, L. Boni, F. Rovera, S. Cuffari and C. Fugazzola, "Microwave tumors ablation: Principles, clinical applications and review of preliminary experiences", *Int. J. Surg.* Volume 6, Supplement 1, pp. S65–S69, Dec. 2008.
- [2] R. C. G. Martin, C. R. Scoggins and K. M. McMasters, "Safety and efficacy of microwave ablation of hepatic tumours: a prospective review of a 5-year experience" *Ann. Surg. Oncol.*, vol. 17, no. 1, pp 171–178, Jan. 2010.
- [3] S. Morikawa, S. Naka, H. Murayama, Y. Kurumi, T. Tani and H. A. Haque, "MRI-Guided Microwave Ablation", in T. Kahn and H. Busse (eds) *Interventional Magnetic Resonance Imaging - Medical Radiology series*, Springer, Berlin Heidelberg, pp. 389-402, 2012.
- [4] K. Shultz, P. Stang, A. Kerr, J. Pauly and G. Scott, "RF Field Visualization of RF Ablation at the Larmor Frequency," in *IEEE Transactions on Medical Imaging*, vol. 31, no. 4, pp. 938-947, April 2012,
- [5] C. Yang, S.Wu, Y. Bai, H. Gao, "Ultrasound monitoring of temperature and coagulation change during tumor treatment with microwave ablation", *J Frontiers of Biology in China*, vol. 4, pp.254-259, 2009.
- [6] S. Zhang et al., "Detection and Monitoring of Thermal Lesions Induced by Microwave Ablation Using Ultrasound Imaging and Convolutional Neural Networks," in *IEEE Journal of Biomedical and Health Informatics*, vol. 24, no. 4, pp. 965-973, April 2020,
- [7] X. Li et al., "Ultrasound Entropy Imaging for Detection and Monitoring of Thermal Lesion During Microwave Ablation of Liver," in *IEEE Journal of Biomedical and Health Informatics*, vol. 26, no. 8, pp. 4056-4066, Aug. 2022
- [8] G. Yang et al., "A Systemic Study on the Performance of Different Quantitative Ultrasound Imaging Techniques for Microwave Ablation Monitoring of Liver," in *IEEE Transactions on Instrumentation and Measurement*, vol. 72, pp. 1-11, 2023
- [9] M. D. Correa-Gallego, A. M. Karkar, and S. Monette, P. C. Ezell, W. R. Jarnagin, and T. P. Kingham, "Intraoperative ultrasound and tissue elastography measurements do not predict the size of hepatic microwave ablations," *Acad. Radiol.*, vol. 21, no. 1, pp. 72-78, Jan. 2014.
- [10] V. Lopresto, R. Pinto, G. A Lovisololo, and M. Cavagnaro, "Changes in the dielectric properties of ex vivo bovine liver during microwave thermal ablation at 2.45 GHz", *Phys. Med. Biol.* vol. 57, no. 8, pp. 2309-2327, 2012.
- [11] R. O. Mays, N. Behdad, S. C. Hagness, "Array Sensitivity for Model-Based Microwave Breast Imaging," *IEEE Trans. Antennas & Propagat.*, vol. 65, no. 6, pp. 100, June 2017.
- [12] M. Lazebnik, M. C. Converse, J. H. Booske and S. C. Hagness, "Ultrawideband temperature-dependent dielectric properties of animal liver tissue in the microwave frequency range", *Phys. Med. Biol.* 51 1941-55, Mar., 2006.
- [13] O. M. Bucci, M. Cavagnaro, L. Crocco, V. Lopresto, and R. Scapaticci, "Microwave Ablation Monitoring via Microwave Tomography: a Numerical Feasibility Assessment", *Proc. of 2016 10th European Conference on Antennas and Propagation*, 2016.
- [14] R. Scapaticci, V. Lopresto, R. Pinto, M. Cavagnaro, and L. Crocco, "Monitoring Thermal Ablation via Microwave Tomography: An Ex Vivo Experimental Assessment", *Diagnostics (Basel)*. 8(4): 81, Dec., 2018.
- [15] M. Wang, L. Crocco and M. Cavagnaro, "On the Design of a Microwave Imaging System to Monitor Thermal Ablation of Liver Tumors," in *IEEE Journal of Electromagnetics, RF and Microwaves in Medicine and Biology*, vol. 5, no. 3, pp. 231-237, Sept. 2021
- [16] M. Haynes, J. Stang, and M. Moghaddam, "Real-time Microwave Imaging of Differential Temperature for Thermal Therapy Monitoring" *IEEE Trans. Biomed. Eng.*, vol. 61, no. 6, pp. 1787–1797, Jun., 2014
- [17] Chen, G., Stang, J., Haynes, M., Leuthardt, E., and Moghaddam, M., "Real-Time 3D Microwave Monitoring of Interstitial Thermal Therapy", *IEEE Transactions on Biomedical Engineering*, vol. 65, no. 3, pp. 528–538, Mar., 2018.
- [18] H. Onal, T. Yilmaz and M. N. Akinci, "A BIM-Based Algorithm for Quantitative Monitoring of Temperature Distribution During Breast Hyperthermia Treatments," in *IEEE Access*, vol. 11, pp. 38680-38695, 2023
- [19] S. Kidera, L. M. Neira, B. D. Van Veen, and S. C. Hagness, "TDOA-based microwave imaging algorithm for real-time microwave ablation monitoring" *International Journal of Microwave and Wireless Technologies*, vol. 10, no. 2, pp. 169-178, Mar. 2018.
- [20] P. M. van den Berg and A. Abubakar, "Contarast Source Inversion Method: State of Art," *Progress In Electromagnetics Research, PIER* 34, 2001, pp. 189–218.
- [21] K. Kanazawa, K. Noritake, Y. Takaishi and S. Kidera, "Microwave Imaging Algorithm Based on Waveform Reconstruction for Microwave Ablation Treatment," *IEEE Transactions on Antennas and Propagation*, vol. 68, no. 7, pp. 5613-5625, July 2020.
- [22] H. Muramatsu and S. Kidera, "TDOA Prior Contrast Source Inversion for Microwave Ablation Quantitative Monitoring" *Proc. 2024 IEEE AP-S Symposium on Antennas and Propagation and USNC-URSI Radio Science Meeting (IEEE APS/URSI 2024)*, July, 2024.
- [23] R. Bracewell, "Pentagram Notation for Cross Correlation.", *The Fourier Transform and Its Applications*. New York: McGraw-Hill, pp. 46 and 243, 1965.
- [24] M. Lazebnik, D. Popovic, L. McCartney, C. B. Watkins, M. J. Lindstrom, J. Harter, S. Sewall, T. Ogilvie, A. Magliocco, T. M. Breslin, W. Temple, D. Mew, J. H. Booske, M. Okoniewski, and S. C. Hagness, "A large-scale study of the ultrawideband microwave dielectric properties of normal, benign, and malignant breast tissues obtained from cancer surgeries," *Physics in Medicine and Biology*, vol. 52, pp. 6093-6115, 2007.
- [25] A. L. Evans, J. F. Sawicki, H. Luyen, Y. Mohtashami, N. Behdad and S. C. Hagness, "Feasibility Study of Microsecond Pulsed Microwave Ablation Using a Minimally Invasive Antenna," *IEEE Antennas and Wireless Propagation Letters*, vol. 20, no. 4, pp. 627-631, April 2021.
- [26] G. Chen, J. Stang, M. Haynes, E. Leuthardt and M. Moghaddam, "Real-Time Three-Dimensional Microwave Monitoring of Interstitial Thermal Therapy," *IEEE Transactions on Biomedical Engineering*, vol. 65, no. 3, pp. 528-538, March 2018.
- [27] Y. Mohtashami, S. C. Hagness and N. Behdad, "A Hybrid Slot/Monopole Antenna With Directional Heating Patterns for Microwave Ablation," *IEEE Transactions on Antennas and Propagation*, vol. 65, no. 8, pp. 3889-3896, Aug. 2017.
- [28] University of Wisconsin Cross-Disciplinary Electromagnetics Laboratory (UWCEM), "Numerical breast phantom repository" [Online]. Available: <http://uwcem.ece.wisc.edu>, accessed on: October 2, 2017.
- [29] L. M. Neira, B. Van Veen, S. C. Hagness, "Strategies for Monitoring Microwave Ablation of Breast Tumors using Microwave Imaging", *Proc. of 2016 IEEE AP-S Symposium*, June, 2016.
- [30] Julius O. Smith III, "Mathematics of the Discrete Fourier Transform (DFT)", *W3K Publishing*, 2003, ISBN 0-9745607-0-7.
- [31] N. Senobari, G. Funning, E. Keogh, Y. Zhu, C. Yah, Z. Zimmerman, A. Mueen, "Super Efficient Cross Correlation (SEC C): A Fast Matched Filtering Code Suitable for Desktop Computers". *Seismological Research Letters*. 90 (1), 2018.
- [32] M. J. Burfeindt, T. J. Colgan, R. O. Mays, J. D. Shea, N. Behdad, B. D. Van Veen, and S. C. Hagness, "MRI-derived 3D-printed breast phantom for microwave breast imaging validation." *IEEE Antennas and Wireless Propagation Letters*, vol. 11, pp. 1610-1613, 2012.



Hideaki Muramatsu received the B.E. degree in Mechanical from University of Yamanashi, Yamanashi, Japan, in 2023. Currently, he is pursuing the M.E. degree with the Graduate School of Informatics and Engineering. His research interests include microwave inverse scattering and ultrasound videos for medical treatment and diagnosis.



Shouhei Kidera (M'11) received his B.E. degree in Electrical and Electronic Engineering from Kyoto University in 2003 and M.I. and Ph.D. degrees in Informatics from Kyoto University, Kyoto, Japan, in 2005 and 2007, respectively. In 2009, he joined as an Assistant Professor with the University of Electro-Communications, Tokyo, Japan, where he is currently a full Professor with Graduate School of Informatics and Engineering in the University of Electro-Communications, Tokyo, Japan. His current research interest is in advanced

radar signal processing or electromagnetic inverse scattering issue for ultra wideband (UWB) three-dimensional sensor or bio-medical applications. He has been stayed at the Cross-Disciplinary Electromagnetics Laboratory in the University of Wisconsin Madison as the visiting researcher in 2016. He has been a Principal Investigator of the PRESTO Program of Japan Science and Technology Agency (JST) from 2017 to 2021. He was a recipient of the 2012 Ando Incentive Prize for the Study of Electronics, 2013 Young Scientist's Prize by the Japanese Minister of Education, Culture, Sports, Science and Technology (MEXT), and 2014 Funai Achievement Award, 2022 KDDI Foundation Award, Contribution Award, and 2023 RIEC Award. He is a senior member of the Institute of Electronics, Information, and Communication Engineers of Japan (IEICE), and the International Union of Radio Science (Union Radio-Scientifique Internationale, URSI), and a member of the Institute of Electrical Engineering of Japan (IEEJ), and the Japan Society of Applied Physics (JSAP).